



# A Method for the Resolution of Simultaneous, Spatially Distinct Absorption Path Measurements Through the Use of Planar Tunable Diode Laser Absorption Spectroscopy

Jacob France\*, Mirko Gamba†

*University of Michigan, Ann Arbor, MI 48109*

With the growth of the optical telecommunications field, Tunable Diode Laser Absorption Spectroscopy (TDLAS) has become a more viable and widely spread method for fluid diagnostics. Traditional TDLAS systems make measurements which are path integrated over a the line-of-sight of a single beam. This work introduces a novel method of taking simultaneous, spatially resolved measurements through the use of sheet forming optics to generate a laser plane instead of a beam. This plane is measured by an appropriate linear array camera (LAC), which makes spectroscopic measurements at each pixel of the array. This work introduces the LAC, noise characterization and initial issues and resolutions for these issues. Three demonstration measurements for the camera are also described: (a) in low pressure cell, (b) over a flat flame McKenna burner, and (c) in a Mach 2.75 wind tunnel. Finally, a Monte Carlo analysis is done on the current absorption features using the noise characteristics taken from the camera. The analysis is run over a range of pressures and temperatures to evaluate the range of validity for the measurements.

## Nomenclature

$I$	Transmitted intensity
$I_o$	Incident intensity
$\alpha$	Integrated absorbance
$\nu$	Wavenumber
$P$	Pressure
$T$	Temperature
$\chi$	Mole fraction of absorbing species
$L$	Path length
$S$	Linestrength
$\phi$	Lineshape function
$\Delta\nu$	Center line Doppler shift
$V$	Fluid velocity
$\theta$	Angle between flow and beam propagation directions
$c$	Speed of light

## I. Introduction

Tunable Diode Laser Absorption Spectroscopy (TDLAS) is a widely accepted method for the measurement of fluid properties. Whereas traditional sampling probes introduce disruptions into flow paths, TDLAS is a non-intrusive technique allowing the flowfield to be measured without significant perturbation.

\*Graduate Research Assistant, Dept. of Aerospace Engineering.

†Assistant Professor, Dept. of Aerospace Engineering, AIAA member.

As the field of optical telecommunications has grown, species of interest for combustion, including H<sub>2</sub>O, CO, CO<sub>2</sub>, and NO, have become easily accessible with off the shelf system components.<sup>1,2</sup> Traditional TDLAS measurements are path integrated along the single line-of-sight (LOS) of the laser beam, which generates measurements at discrete points. This work introduces a novel method for taking planar tunable diode laser absorption spectroscopy (PTDLAS) measurements, from which simultaneous, spatially-distinct absorption paths can be obtained. By taking measurements over a plane instead of a single path, this method generates measurements over a line instead of at a single point.

To accomplish this, the incident laser beam is expanded into a two-dimensional (collimated) plane using sheet forming optics. The transmitted light from this plane is measured with a suitable linear array camera (LAC). Scanned-wavelength direct absorption measurements are made at each pixel in the array. In this way, a (path-integrated) line measurement, rather than a point measurement, is made through the flowfield. As improvements in LACs are made, this approach has the potential to extend to wavelength modulation techniques. Furthermore, this method can be extended to volumetric measurements using the same concept as improvements to suitable (e.g., near infrared red) high-framing rate cameras become available. To demonstrate this approach in this work, we use a near-infrared (NIR) laser to measure well known H<sub>2</sub>O transitions near 1.39  $\mu\text{m}$  in three well controlled settings: (a) a uniform pressure, temperature, and species fraction low pressure cell; (b) a uniform pressure, variable temperature and species fraction flat flame McKenna burner; and (c) a uniform pressure, temperature, and species fraction wind tunnel to measure the Doppler shift. In addition, we perform characterization on the camera in order to obtain noise characteristics, which are then used in a Monte Carlo simulation analysis to evaluate the range of validity of the measurements. These results are then used to identify the limitations of the method and selected transition lines.

## II. Background

Atoms and molecules have specific and distinct absorption bands that can be accessed by light at well-defined wavelengths. TDLAS is a method that relates incident and transmitted intensities to the absorption properties of the target species through Beer's Law:

$$I/I_o = \exp \{-A(\nu, P, T, \chi, L)\} \quad (1)$$

where  $A$  is the spectral absorbance, which is a function of the wavenumber  $\nu$ , pressure  $P$ , temperature  $T$ , the mole fraction of the absorbing species  $\chi$ , and the path length  $L$  along the LOS. The spectral absorbance  $A$  can be written as:

$$A = \int_0^L \sum_i S_i(T) P \phi_{\nu,i}(\nu, P, T) \chi d\ell \quad (2)$$

where the integral is over the absorption path (where in general  $P$  and  $T$  may vary along the path) and the summation is for a series of individual transitions  $i$ . The integrated absorbance  $A$  is then computed by spectrally integrating  $A$  over the spectral range of interest.  $S_i(T)$  is the linestrength, and  $\phi_{\nu,i}$  is the lineshape function, which is a spectral quantity that is a function of pressure and temperature, for a transition  $i$ . Under many conditions,  $\phi_{\nu}$  can be represented by the Voigt lineshape function, which is a convolution of the Gaussian (which describes Doppler broadening) and the Lorentzian (which describes collisional broadening) lineshape functions. In addition, the implementation of the Voigt lineshape function is relatively simple and is therefore often used. In this work, we adopt the Voigt function approximation of Humlíček-Weideman<sup>3</sup> to improve the computational performance of some of the analysis we conduct. The parameters for the Voigt profile are taken from the HITRAN database.<sup>4</sup>

For the case that properties are uniform along the LOS, the ratio of the integrated absorbance of two distinct absorption lines,  $A_i$  and  $A_j$  with  $i \neq j$ , can be used to obtain the gas temperature. In this case, the dependence on pressure and absorbing species mole fraction cancels out, leaving temperature as the only unknown through the ratio in linestrength on the two absorption line selected:

$$R = A_i/A_j = S_i(T)/S_j(T) \quad (3)$$

Previous work has investigated strategies to maximize measurement sensitivity and accuracy.<sup>5</sup> Furthermore, given this temperature and the width of the absorption feature, pressure can also be determined, leaving the

mole fraction as the only unknown. Then using the integrated absorbance of only one absorption line, the mole fraction can be calculated according to:

$$\chi = A_i/S_i(T)PL \quad (4)$$

In this manner, the properties of the flow field are found.<sup>6-8</sup> Due to the limitations in the measurement of spectral absorbance, it is typically difficult to obtain accurate measurements using the direct absorption method. Therefore, alternative methods based on wavelength modulation have been developed for the determination of the gas state.<sup>9-11</sup> In this work, we adopt direct absorption despite these known difficulties, and we follow the method outlined here as an initial proof-of-concept for the use of the LAC for TDLAS measurements. Direct absorption also helps overcome some of the acquisition rate limitations of the current LAC that prevent the extension of the current methodology to the more robust wavelength modulation strategies.

Another possible measurement that can be made using TDLAS is velocimetry, which is done by making use of the Doppler shift of the line center of the absorption feature as the laser propagates through a moving gas. By measuring the relative shift, one can determine the flow speed according to:

$$\Delta\nu = \nu_o \frac{V \cos \theta}{c} \quad (5)$$

where  $\Delta\nu$  is the shift in the absorption features,  $\nu_o$  is the actual line center of the absorption feature,  $V$  is the flow speed,  $\theta$  is the angle between the flow and the propagation direction of the beam, and  $c$  is the speed of light.<sup>12</sup>

In this study, we focus on evaluating the approach for the measurement of pressure and temperature at discrete positions along the measurement line, while we will evaluate its capability in measuring Doppler velocimetry in later work.

### III. Experimental Considerations for Linear Absorption Measurements

#### A. Experimental Setup

Measurements are made in controlled environments to assess the validity of the camera as a detector for PTDLAS. The experimental setup for the three tests is similar with the exception of the testing region through which the beam passes. The general schematic for the setup is seen in Fig. 2. The necessary laser beam is generated by an DFB diode laser (NEL NLK1E5GAAA, 20 mW power) and it is split four-ways by a  $1 \times 4$  beam splitter. Two beams are used for the absorption measurements using two different detection systems, one One beam is passed through the sheet forming optics to the linear array camera while a second is passed through an etalon for the determination of wavelength variation with time. A third beam is passed directly to a detector, and it is used to determine the reference signal for the undisturbed laser intensity,  $I_o$  (i.e., to measure the laser baseline); we refer to this third beam as the “baseline”. The fourth beam is used for traditional single line measurements; its use varies by the testing environment and will be described for each case.

The experimental setup is composed of two detection systems. The first system is the traditional single beam configuration which uses traditional fiber-coupled pitch and catch optics, an InGaAs photodetector, and is measured with a high speed 14 bit digitizer. The second system is used to generate the planar measurements. This system is comprised of off-the-shelf cage system components and optics to form the beam into a collimated plane. The laser pitch assembly is a combination of -6.25 mm focal length plano-concave lens and a 125 mm focal length plano-convex lens. Both of these optics are anti-reflection (AR) coated to minimize back reflections which can result in etalon noise. The first of these lenses spreads the beam one-dimensionally into a fan, while the second collimates the fan into a sheet approximately 20 mm wide. This assembly is enclosed in a tube and continuously purged with nitrogen to minimize unwanted absorption from moisture in the ambient room air. The laser sheet catch assembly is composed of a 50 mm focal length plano-convex cylindrical lens that focuses the incoming sheet onto the linear array. Unwanted light (flame luminosity, ambient light, etc.) is rejected by the application of an optical bandpass filter centered around the laser wavelength and a slit. These components are also enclosed and purged with nitrogen.

A DFB tunable diode laser (NEL NLK1E5GAAA, 20 mW power), producing wavelengths near 1388 nm in the Near Infrared (NIR), is used to access the absorption lines of  $H_2O$  at  $7203.890 \text{ cm}^{-1}$ ,  $7203.894$

$\text{cm}^{-1}$ ,  $7204.166 \text{ cm}^{-1}$ , and  $7205.246 \text{ cm}^{-1}$ . The first two lines are nearly at the same wavelength and have approximately the same lower state energy, and so are treated as one line by summing their corresponding linestrengths. The laser diode controller used to drive the tunable diode laser provides a modulation current that produces a nearly linear variation of the laser output wavelength within the intended scan range. The acquisition rate of the camera is synchronized with external instrumentation at  $46.816 \text{ Hz}$ , and images are captured with a frame grabber. The wavelength variation in time over a scan is determined through an etalon signal. A schematic diagram of the experimental arrangement used to generate and acquire linear absorption measurements is shown in Fig. 1. The individual line images taken by the LAC are then "stacked" together to generate a two-dimensional representation of the scan (i.e., images). In these images, the horizontal axis represents spatial information (pixel value) and the vertical axis represents temporal information, which is then converted to (absolute) illumination wavenumber using the etalon measurements and reference calibration against known absorption line positions. An example of the measured linear distribution of the absorption scan centered on the selected absorbance feature of  $\text{H}_2\text{O}$  is shown in Fig. 3. The resulting images are processed to extract the spectral absorbance from individual pixels and by averaging groups of pixels. For example, the resulting absorption scan as measured by integrating across the linear array is shown to the right of the absorption scan image in Fig. 3.

## B. Sheet Forming Issues and Solution

As noted previously, the sheet forming optics are AR coated to help suppress etalon noise. Etalon noise occurs when back reflections off of optics introduce constructive and destructive interference during laser scans. As more optics are added to a system, the probability of etalon noise increases as there is a chance for reflections off of each surface. These interference patterns appear as high frequency modulation of the raw absorption scans and are carried over as systematic noise in the spectral absorbance profiles. This causes problems in the reconstruction of flow properties as even a 1% etalon signal can generate a 3% error in temperature, and a 1% error in absorbing species fraction using the data reduction method outlined here. As seen in Fig. 4, the etalon noise that appears in a single pixel scan can be reduced by averaging, but not eliminated. Because we seek to conduct measurements at individual (or a small group of) pixels, it is critical to reduce etalon noise as much as possible, ideally well below the 1% contribution limit.

In order to accomplish this goal, several techniques have been attempted. First, the optics were arranged to eliminate planar surfaces to face each other to avoid back reflections that would introduce interference effects. This allows for a clean image over 90% of the plane. However, there are still locations where etalon interference exists. This can be seen in the Fig. 5 where (for each subfigure) the image of the raw absorption scan signal acquired using the lens-based system (lower image) is shown along with the scan signal extracted at one single pixel (plot on the right, with lines extracted at two different locations along the sheet shown in 5(a) and 5(b)). The line labeled "*Lens-based*" refers to the initial lens-based sheet forming configuration.

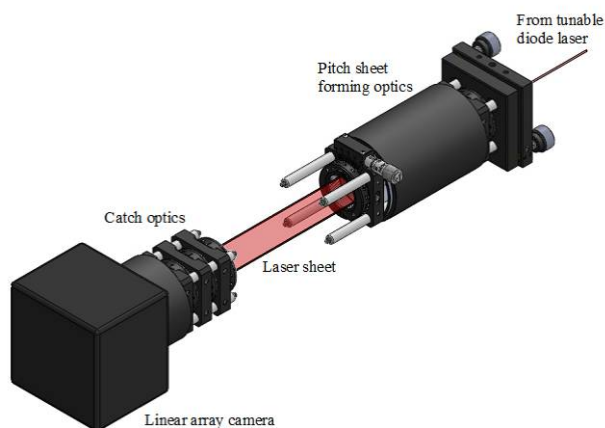
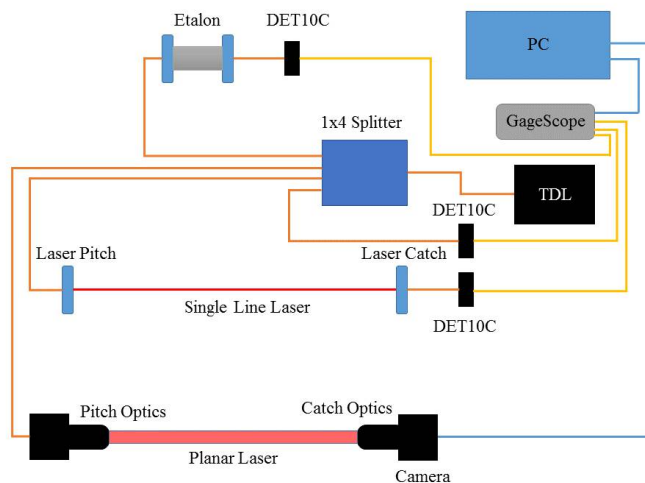


Figure 1. Schematic diagram of the experimental arrangement for planar TDLAS measurements.



**Figure 2. Schematic diagram of the general experimental setup used for the three demonstration measurements.**

An alternative way to form a sheet that we explored was to use a pair of anamorphic prisms arranged to generate a magnified laser beam in one direction by a factor larger than unity, while maintaining co-linearity between the incoming and expanded beam. The prism pairs offer no parallel surface pairs where reflections can generate interference effects, thus completely eliminating etalon effects. The upper image in each case of Fig. 5 refers to the scan image generated with the prism-based system. The resulting scan at one pixel location is correspondingly shown in the plot and it is labelled “*Prism-based*”. The lack of etalon noise is clearly evident in the raw signal. By matching two sets of these anamorphic prisms, up to 25x magnification of the laser can be created along a single dimension, thus expanding the initial beam sufficiently to fully illuminate the array sensor without the problem of etalon noise. Based on the initial success with a single prism pair at a magnification of about 5, we are currently designing a two-pair system to generate the necessary 25x magnification for future evaluation and use. What shown here is based on the lens-based system, however. Thus, some etalon effects are present.

### C. Camera Characterization

A camera characterization study was completed to assess the noise characteristics of the camera. This is necessary to better understand the performance and limitations of the linear array camera arrangement and to identify opportunities to optimize the configuration. Of particular interest is to evaluate the linearity of the sensor array and its noise characteristics, for example under conditions of varying irradiance but fixed exposure times such as one would observe during the absorption scan. When scanning over an absorption transition in scanned-wavelength direct absorption measurements of the type considered here (see for example Fig. 5), the irradiance varies with wavenumber (i.e., over the scan), while the exposure time and any other settings of the camera remain constant. This causes a variation in signal-to-noise ratio (SNR) over the course of the scan. In order to characterize the noise, an integrating sphere is used to produce a uniformly illuminated plane, which is measured by the LAC. The TDL illumination is fixed and set to be off of any  $\text{H}_2\text{O}$  transition lines. The laser is passed through a ground glass window (with an NIR transmission of near 50%) to spread the beam before entering the integrating sphere. Images are taken by the LAC at an exposure time of  $177 \mu\text{s}$  over ten evenly spaced irradiance values corresponding to 10% to 100% of the maximum laser power. Dark images taken without the presence of the laser are used to correct the image by removing ambient light. This range is representative of the illumination that occurs during a typical absorption scan used in the current work. Testing was done for the low and medium gain settings for the camera at a linescan rate of 5,526 lines/s. Testing was attempted at high gain, but the LAC was saturated, preventing measurements.

The images taken are temporally averaged over 5000 samples, and the SNR is plotted against the photo-

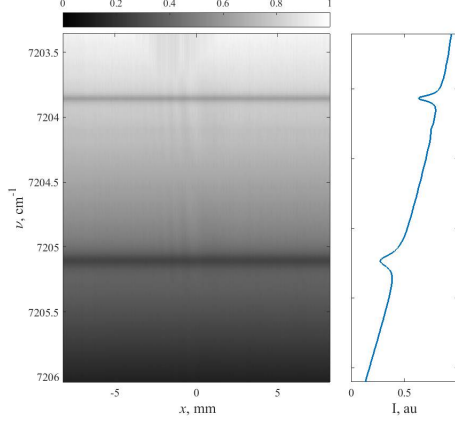


**Figure 3. Example of linear measurement of an absorption scan. The profile on the right is frame-averaged absorption scan.**

electrons measured by the camera. As can be seen in Fig. 6, the SNR increases with both the photoelectrons captured and with increasing gain. The photo-electrons  $\psi$  are estimated from the irradiance as:

$$\psi = Q \frac{\lambda}{hc} A_p B P'' \Delta t \quad (6)$$

$Q$  is the quantum efficiency of the camera,  $\lambda$  is central wavelength of the illumination laser (1.38  $\mu\text{m}$ ),  $h$  is Planck's constant,  $c$  is the speed of light,  $A_p$  is the physical pixel size,  $B$  is the pixel fill factor,  $P''$  is the laser irradiance illuminating the detector, and  $\Delta t$  is the exposure time. The SNR is modeled accounting for shot noise, dark noise and readout noise according to:

$$SNR = \frac{\frac{\psi}{GQ}}{\sqrt{Q\psi/G^2 + \sigma_{dark}^2 + \sigma_{ro}^2}} \quad (7)$$

where  $G$  is the gain setting of the camera,  $\sigma_{dark}$  and  $\sigma_{ro}$  are the the dark and readout noise, respectively. Estimates of dark and readout noise were taken from data provided by the manufacturer. The noise characteristics obtained through this characterization are used in the Monte Carlo simulation, described in section 5, to generate representative LAC measurements with realistic SNR values.

Another limitation of the LAC was identified during this testing. Under nominally uniform irradiance, alternating pixels output “high” and “low” signals as demonstrated in Fig. 7. During instantaneous measurements, random noise obscures this, but the alternating signal structure remains after temporal averaging. It is possible that this could influence measurements. Currently, two sets of profiles are generated by straddling the “high” and “low” signals, then averaging them together. This binning somewhat reduces pixel noise, but halves the spatial resolution of the LAC system. This effect appears to be associated with the design of the sensing array, but is not expected to prohibit measurements if properly accounted for.

## IV. Demonstration Measurements

Measurements are made in controlled environments to assess the validity of the camera as a detector for PTDLAS. The experimental setup for the three tests is similar with the exception of the testing region through which the beam passes. The general schematic for the setup is seen in Fig. 2. The laser beam itself, generated by an DFB diode laser (NEL NLK1E5GAAA, 20 mW power), is passed through a  $1 \times 4$  beam splitter. One beam is passed through the sheet forming optics to the linear array camera while a second is passed through an etalon for the determination of wavelength variation with time. A third beam is passed directly to a detector, and it is used to determine the reference signal for the undisturbed laser intensity,  $I_o$  (i.e., to measure the laser baseline); we refer to this third beam as the “baseline”. The fourth beam is used

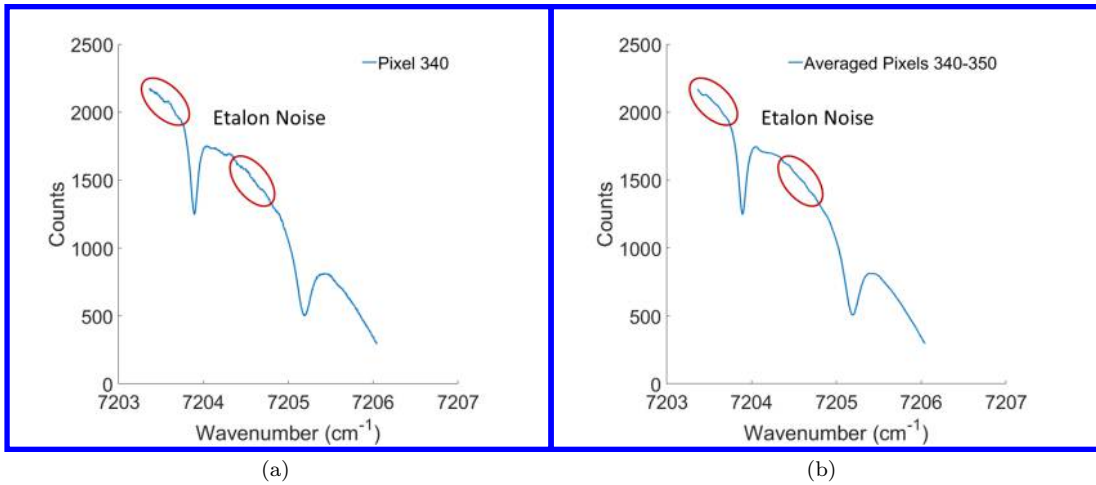


Figure 4. Comparison of etalon noise in (a) a single pixel vs (b) over a 10-pixel average bin. The etalon noise is reduced with averaging, but not eliminated.

for traditional single line measurements; its use varies by the testing environment and will be described for each case.

### A. Low Pressure Cell

Data is gathered in a low pressure absorption cell using both the traditional single line techniques as well as the LAC.  $I_o$ , obtained from the baseline, is used to extract the spectral absorbance from measurements of the type in Fig. 3. Measurements are taken through the cell with both systems and signal are corrected for both using dark images taken with the laser off. Initially, the absorption cell is capped at ambient conditions. The cell is then pumped down through a series of steps to the desired pressure values to ensure that the species fraction of  $H_2O$  remains constant throughout the duration of the tests. Simulations of the spectra are generated using parameters from the HITRAN database and the known conditions within the cell. The single line scans are used to verify the accuracy of the simulation. This simulation is then used to validate the camera measurements and is implemented in a Monte Carlo simulation described in Section 5. The schematic of the low pressure cell experimental setup is seen in Fig. 8. The pressure cell conditions are measured by an MKS Baratron (Type 626C) which is connected to the absorption cell to measure absolute pressure. Relative humidity and temperature in the room air are measured from an SK Sato Datalogger, which allows for knowledge of the relative humidity to within 0.1%, and temperature to within 0.1°C. In order to obtain adequate wavenumber resolution and signal to noise ratio (SNR), line images are taken at a rate of 46,816 lines/second with an exposure time of 17.4  $\mu s$ . The linescan rate and exposure are chosen such that that images obtained are neither saturated nor underexposed.

Conditions used for the single line scans are given in Table 1. Fig. 9 shows the spectral absorbance averaged over 100 scans measured through the low-pressure absorption cell for the three single line cases shown in Table 1. The spectral absorbance profiles are superimposed on simulated profiles using the Voigt lineshape function calculated from HITRAN parameters and the conditions listed in Table 1. At all three pressures, the simulations accurately match the single line scans. In addition the pressure shift is measurable using the single line scans and can be seen in Fig. 10(a), while the difference error between the calculated shift and the measured shift can be seen in Fig. 10(b). Thus, comparison to the simulation is a good measure of the accuracy of the measurements with the camera setup.

The LAC is tested at approximately the same conditions as the single line, which can be seen in Table 2. A baseline image is taken when the LAC is connected to an  $N_2$  purge, which is then used as  $I_o$  in order to extract the spectral information from the camera images. By taking the scan measured at each pixel and using the corresponding baseline image pixel scan, the spectra can be reconstructed across the entire image. The baseline images must be corrected due to a slight offset. This offset is less than 1% of the signal, but if left uncorrected leads to errors in the wings of the spectra. The new image generated during this process

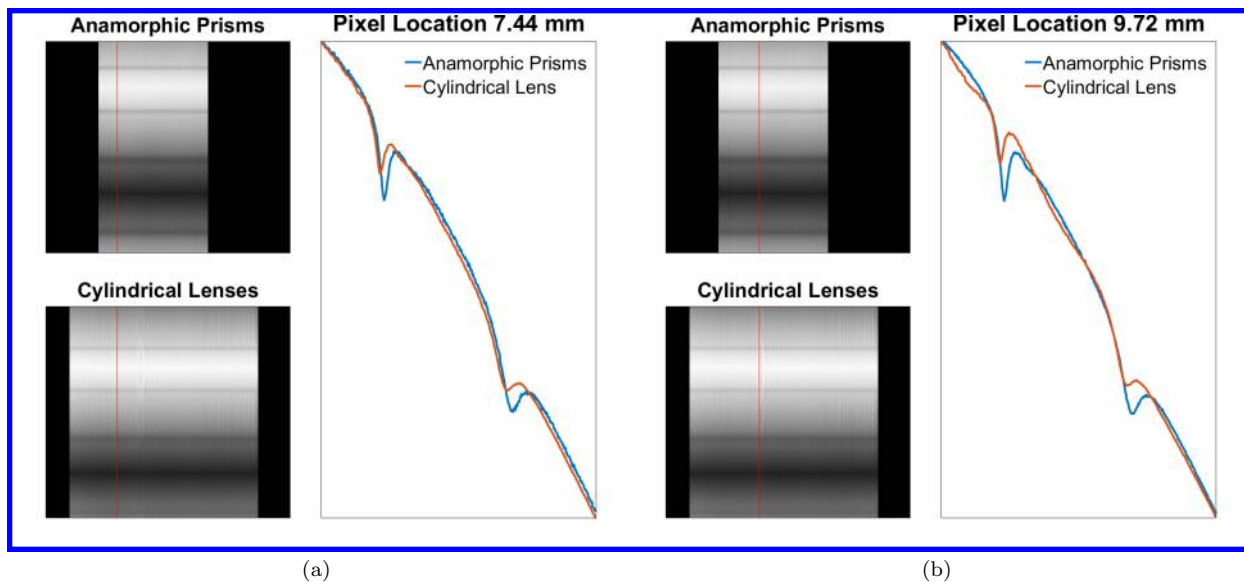


Figure 5. Comparison of the performance of the lens-based (combination of plano-convex and plano-concave cylindrical lenses) and the anamorphic-prism-based sheet forming systems on capturing an etalon-free absorption scan. A clean section of the image is seen in (a) while etalon effects are seen in (b).

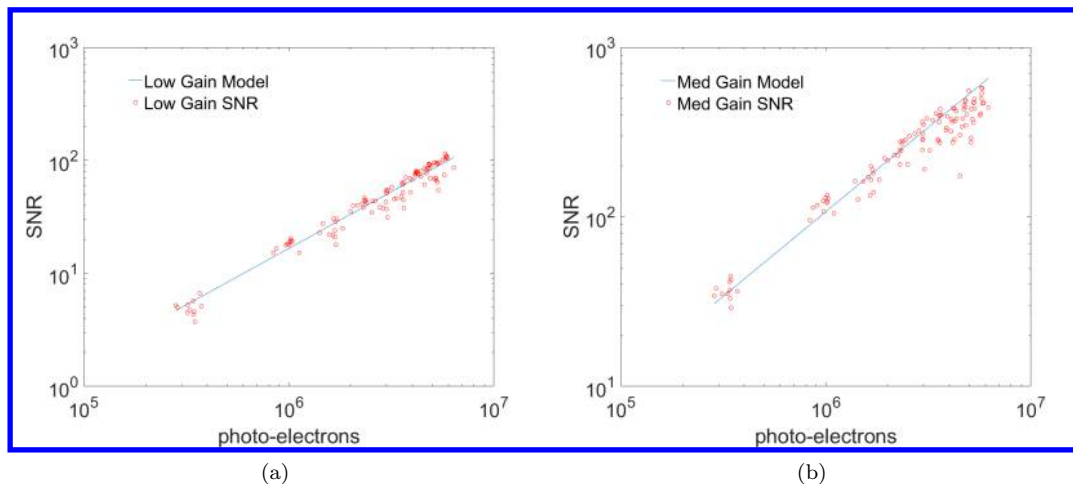
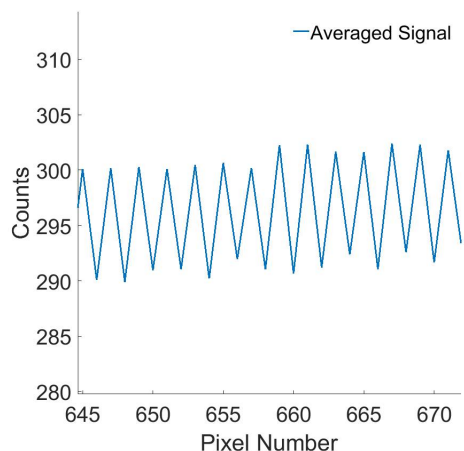


Figure 6. SNR as a function of photo-electrons for the (a) low and (b) medium gain settings of the linear array camera with the model results (solid line) superimposed on the measured data.

is referred to as the “spectral image”. The spectral images generated for the conditions shown in Table 2 are shown in Figure 11. In these spectral images, the vertical axis indicates wavenumber and the horizontal axis indicates the spatial distance along the measurement plane (i.e., across the linear camera array). Note that unlike the spectra measured with the single line setup, the spectral images are single scan realizations, not multiple scan averages. Alongside each spectral image, the line-averaged absorption spectrum obtained by averaging the spectral absorbance along the spatial direction is shown (red solid line) and compared to the simulated spectrum from HITRAN (blue solid line).

The generated simulated spectra match well with the averaged profiles. However, we intend to take measurements with good spatial resolution, so measurements over individual pixels (or over a small number binned pixels) need to be accurate. This accuracy is demonstrated in Fig. 12, where the spectra from a single



**Figure 7.** Alternating pixels produce “high” and “low” signals which are normally overwhelmed by random noise, but remain after temporal averaging.

pixel (0.025 mm spatial resolution), an average over 5 pixels (0.124 mm effective spatial resolution), and an average over 10 pixels (0.248 mm) are compared to the generated spectra. Note that the shape and value of the absorption lines remains constant, although the noise decreases with averaging. This demonstrates that the individual pixels are able to capture the absorbance spectra, and that binning is a possible method of noise suppression. Each of the plots also displays the spectra measured at two locations on the array. These spectra vary slightly due to the slight variation of intensity across the laser sheet. The offset used in generating the spectral images assumes that the laser intensity does not vary in space. By obtaining a more accurate representation of the baseline offset, it is expected that these spectra will collapse better to the generated HITRAN spectra.

The root-mean-squared (RMS) error was calculated for the difference between the measured absorption spectra measured at a single pixel, 5-pixel, and 10-pixel bins and the HITRAN simulated spectra over a range of temperature and pressure. The temperature ranged from  $\pm 5\%$  of the nominal temperature, 294 K. Pressure ranged from  $\pm 10\%$  of the nominal pressure, 47.8 kPa. Contour plots of the RMS error are given in Fig. 13. The single pixel measurements give a region of minimum error that is slightly different than the nominal values, approximately 4.6% and 1.3% difference for pressure and temperature, respectively (reported

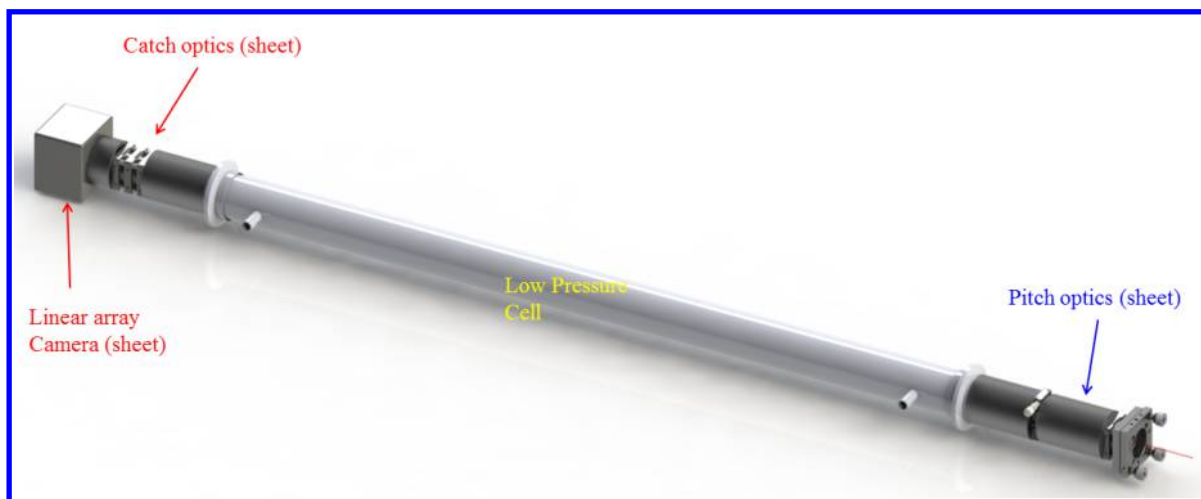


**Figure 8.** Schematic diagram of the low-pressure cell measurement experiment.

Case	Temperature, K	Pressure, kPa	H <sub>2</sub> O Mole Fraction
A	295	30.0	0.0085
B	295	60.0	0.0085
C	295	99.3	0.0085

Table 1. Summary of conditions used in single line scan measurements.

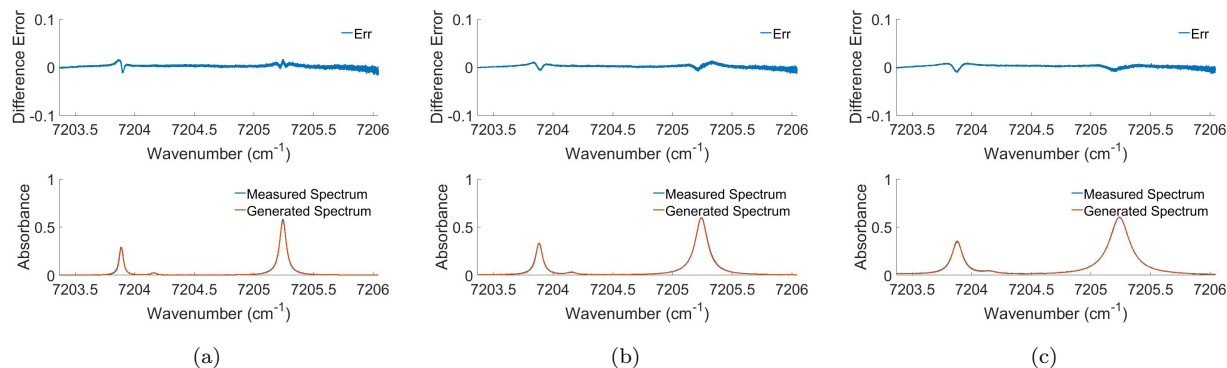


Figure 9. Spectral absorbance measured with the single line system through the low-pressure absorption cell at a pressure of (a) 30.0 kPa, (b) 60.0 kPa, and (c) 99.3 kPa superimposed on a numerically generated profile using values in Table 1 and HITRAN spectroscopic parameters.

values at 45 kPa and 290 K). The region of minimum error for the 10-pixel average case is very close to the known conditions of 47.8 kPa and 294 K. Thus, the camera is a viable method for taking spectroscopy measurements, even on a single pixel basis.

The pressure shift is measured with the camera as well, though with poor initial results. As seen in Fig. 14(a), the shift measured by the camera, superimposed on the calculated shift is a poor match (although the trend is correct). There is an outlier measured at 100 kPa that does not fit the trend correctly. Fig. 14(b) shows the difference error between the measured and calculated shifts. These measurements were completed at a relatively low linescan rate, which produces low wavenumber resolution. By increasing the resolution, it is possible that the measured pressure shift will become more accurate. This will be addressed in future work.

## B. Flat Flame Measurements

Initial measurements are made over a 6 cm flat flame McKenna burner for a hydrogen/air flame. By orienting the LAC so that the laser sheet is vertical, simultaneous measurements of the spatial variation of the temperature and species mole fraction should be able to be made, resulting in instantaneous profile measurements above the surface of the burner. The schematic for this arrangement in the experimental setup can be seen in Fig. 15. Data is taken with both the traditional single line and with the LAC. The single line data is shown in Fig. 16. In the current setup, the beam passes through both ambient air and the flame. A nitrogen curtain separates the flame from the ambient air, stabilizing it and preventing the edge

Case	Temperature, K	Pressure, kPa	H <sub>2</sub> O Mole Fraction
D	295	28.6	0.0070
E	295	57.4	0.0070
F	295	98.3	0.0070

Table 2. Summary of conditions used in LAC measurements.

of the flat flame from mixing and reacting with the ambient air. The room conditions are measured in the same manner as for the low pressure cell and are accounted for in the HITRAN simulation and fitting. Also similar to the low pressure cell, an error contour was made for varying temperature and species fraction of the flame profile as seen in Fig. 17. In this temperature and species fraction range, the region of minimum error is long and narrow. This occurs because the increase in temperature effectively reduces the linestrength for this condition. By increasing the mole fraction, the reduction in the peak absorption can be "cancelled" out, generating nearly the same absorption feature. This means that as the temperature is increased, if the mole fraction correctly, the absorption spectrum that is generated is nearly the same. This results in a long, narrow region of minimum error. For future flame measurements, it may be necessary to add additional constraints in order to accurately determine the properties. For stoichiometric conditions the expected flame temperature is 1900 K, while the expected species mole fraction of  $\text{H}_2\text{O}$  is approximately 0.34. This point does not fall in the region of minimum error. This deviation could result from the burner not running at stoichiometric conditions, which could produce differences in temperature and species fraction from the expected stoichiometric values.

Measurements are attempted by the LAC system over the McKenna burner as well. These measurements were taken at a  $17.4 \mu\text{s}$  exposure time and a linescan rate of 46,813 lines/s. However, limitations that prevented useful data from being gathered have been discovered. The LAC is sensitive from approximately 0.95 microns to 1.7 microns. This is useful in that it provides access to many lines that fall within that broad range. However, it also means that broadband NIR emission, such as that from a flame, tends to contaminate or even saturate the array. In order to reduce the flame background emission, a bandpass filter centered at 1375 nm with a full-width at half-maximum of 50 nm is employed, which blocks the majority of the excess flame emission. A slit appropriately sized and placed in front of the sheet collection optic of the LAC system is also used to further block unwanted light, other than the laser illumination plane. The use of a slit is found to be very effective in reducing the collection of flame luminosity. The combination of the bandpass filter and the slit has helped to reduce flame luminosity to acceptable levels. In addition, a high extinction NIR polarizer has been tested, which further reduces the interference from flame luminosity, but also introduces etalon noise, and so has been seldom used in measurements so far.

Another limitation is that the variations that appear in the image taken by the camera produce artifacts in the absorbance profiles. Fig. 20 shows a raw scan taken at 9.23 mm above the surface of the burner. Also seen on that plot are spectra gathered from pixel averaging which demonstrate the reduction in the artifacts that appear in the profile. This is believed to be caused by beam steering that occurs when spatial variations in density cause a deflection of the propagation beam. Line-of-sight variations of fluid density above the flat flame can occur in both time and space. This can cause significant variations in measured laser intensity, thus introducing artifacts in the reconstructed spectral absorbance that effectively reduce the overall SNR of the measured absorbance and induce errors in the reconstruction of the temperature and species fraction. Quantification of this aspect is ongoing, and will be further explored in future experiments on flat flame burners.

The spectral image for the flat flame can be seen in Fig. 18. The horizontal axis represents the height above the burner surface (HAB), while the vertical axis represents the illumination wavenumber. This variation in the spectra can be seen in Fig. 19. The spectra are single pixel measurements which vary with the HAB. The variation in the spectra reflects the change of temperature and species fraction across the flat flame above the McKenna burner. The artifacts highlighted in Fig. 20 from the beam steering currently prevent acquisition of accurate measures of temperature and species fraction from the images. However, the difference in profiles demonstrates the capability of the LAC to make such measurements once the beam steering issues have been resolved.

### C. Wind Tunnel Measurements

Wind tunnel measurements are currently ongoing. Measurements will be made in the University of Michigan's Mach 2.75 indraft wind tunnel. Indraft tunnels have an advantage over blowdown tunnels in that the pressure in the test section is lower than ambient because the absorption lineshape is narrower at lower pressures, which allows for easier baseline fitting and causes the spectra to be visible even in the presence of minimal absorbing species. Thus, spectra are visible without the need for external seeding of the tunnel. The cross-sectional area of the tunnel is 57.2 by 69.3 mm with 106.7 cm long glass walls for optical access and measurements are made 45.72 cm from the throat. The single line laser is passed nearly perpendicular to the flow, while the LAC is passed at  $45^\circ$  angle. The LAC is nitrogen purged to remove

ambient air effects. By passing both beams through the flow, the resulting measurements are free of pressure shift effects. The pressure shift measured in the low pressure cell is on the order of the Doppler shift expected from the Mach 2.75 wind tunnel. The pressure shift is distinguishable in these pressure cell measurements, providing proof of concept that the Doppler shift should be measurable. The expected Doppler shift under normal conditions for the Mach 2.75 wind tunnel is approximately  $0.008 \text{ cm}^{-1}$ . The schematic of the current wind tunnel experimental setup is seen in Fig. 21.

Two issues are observed in the initial datasets taken in the wind tunnel. The first problem is that there are large etalon features in the absorption spectra. This is easily corrected by shifting the perpendicular line by a few degrees. This small angle is accounted for in processing. Another cause of etalon effects comes from a film which can form on the inside of the windows. The tunnel is used for PIV measurements and the oil used to seed the tunnel can coat the optical access windows. When this occurs, the film acts as an etalon, generating the usual constructive and destructive interference patterns in the scans, as well it deflects the beam or partially obscures the optical path. This is avoided by regularly cleaning the windows, ensuring that the film does not build. The second problem is that the purge system is not adequate. Initial measurements made consist of mainly room air absorption, which drowns out most of the absorption seen inside the tunnel. Careful processing reveals a shift is present, but the error between the measured and calculated shift is on the order of 50%, which is unacceptably large. This results in the need for a new purge system which is currently being designed.

## V. Monte Carlo Simulation

A numerical assessment of the expected accuracy of the measurement approach under different conditions is carried out using a Monte Carlo analysis approach specific to the measurement conditions currently used. The objective of the analysis is to determine the accuracy of the data reduction method, as well as to evaluate the range of conditions over which the method is valid taking into considerations limitations and strengths of the imaging setup currently used. As we expand on the scope and capabilities of this assessment in our future work, we will aim at optimizing the method including other accessible absorption lines or alternative measurements configurations.

The analysis is based on reconstructing synthetic absorption data that accounts for noise and averaging effects of the LAC approach, from which the thermodynamic properties are reconstructed and compared with the known quantities in a Monte Carlo framework. First, the analysis generates a baseline laser (temporal) profile using Eq. 6. The laser power is assumed to be a linear profile that varies from 100% to 10% of the maximum laser power. The arriving photons are integrated over the exposure time to simulate the LAC acquisition. Using the gain supplied by the manufacturer, the photoelectrons are converted into counts. Absorbance spectra are generated using HITRAN simulations over a range of pressure and temperature and at a  $45^\circ$  angle of incident to a high speed flow to generate a Doppler shift. These simulations are run external to the routine generating synthetic absorption scans and saved in order to reduce processing time. From Beer's Law, the simulated spectrum multiplied by the baseline gives the transmitted light. An example of this raw transmission signal is given in Fig. 22. Subsequently random noise is added to this signal by generating the standard deviation of the noise through the equation seen below.

$$NOI = \sqrt{\sigma_{shot}^2 + \sigma_{dark}^2 + \sigma_{ro}^2} \quad (8)$$

This noise profile is used to create Gaussian curves with the same standard deviation, which are used to generate random noise that is added to the transmitted signal, which replicates the measurement taken by the LAC. By using the noise characteristics of the LAC system extracted from initial camera characterization we attempt at generating a realistic synthetic signal that would be measured by LAC.

In actual measurements, the baseline is measured directly by a detector and a line is fit to it in order to suppress random noise in the baseline. The Monte Carlo algorithm uses the simulated baseline to represent this fit. Using Beer's Law, the simulated baseline, and the noisy transmitted signal, the "measured" absorption spectrum is calculated. An example of a synthetic spectrum is shown in Fig. 23, where the HITRAN spectrum is superimposed on the simulated spectral absorption profile. Using this profile, either temperature, pressure and species mole fraction or velocity can be reconstructed using the traditional techniques described in Section 2 of this work. The error is obtained as the difference between the reconstructed and known values. A "region of validity" is defined as the region in  $(P, T, \chi_{H_2O})$  space where there is an 85% probability that the reconstructed solution is under a 10% error. Figures 24(a), 25(a), 26(a), and 27(a) show

the probability that the reconstructed values for temperature, pressure, species fraction, and velocity will be within 10% of the known value. The data is taken over a range of eight evenly spaced pressure values from 20 kPa to 130 kPa. Figures 24(b), 25(b), 26(b), and 27(b) also show the probability that the reconstructed values for temperature, pressure, species fraction, and velocity are within 10% of the known values, but the data is taken over a range of five evenly spaced temperature values from 300 K to 1050 K.

The range of validity varies by pressure and temperature combinations. For example, for pressure ranges from 100 kPa to 130 kPa, the region of validity includes the temperature values from 300 to 1000 K, whereas the region of validity for 25 kPa only includes temperature values from 300 to 700 K. These regions can be defined for all the reconstructed properties. However, it is evident that the combinations that produce narrower absorption peaks have larger errors than the broader features. On every plot, as the temperature increases, the probability of accurate reconstruction decreases. As the pressure decreases, the probability of accurate reconstruction also decreases. This is attributed to two reasons. The numerical integration method used to compute the integrated absorbance from the spectral distribution in the reconstruction sequence is trapezoidal integration. As the absorption lineshape becomes narrower, the error introduced by this method increases. In addition, as the absorption lineshape becomes narrower, the random noise can have a larger effect on the result of integration. Also note that the accuracy of the method decreases from temperature, to pressure, to mole fraction. This is due to the fact that the errors propagate through the solution. Temperature is reconstructed first, then used to obtain the pressure. Therefore, any errors in temperature are carried into the pressure solution. Both temperature and pressure are used to solve for the mole fraction of the absorbing species, meaning the errors from both quantities are carried into the solution for species mole fraction. This is possibly the reason why the reconstructed temperature is valid over a much larger region than pressure or species mole fraction. It should be noted that by increasing the wavenumber resolution of the scan, it is expected that the errors will decrease. Likewise, by improving the SNR of the measurements, the errors are expected to decrease. The wavenumber resolution of the scan is easily corrected by using a higher linescan rate from the camera and/or operating on the exposure time. It is also possible to increase the SNR by using longer exposure times or higher gain settings, but this needs to be evaluated based on camera saturation limitations. Additional future work is directed on evaluating and quantifying these aspects and improve on the measurement capability.

## VI. Conclusion

This work demonstrates the validity and early applications of planar tunable diode laser absorption spectroscopy where the traditional single-point, path-integrated measurement of fluid properties through the absorption of laser light by a suitable species is extended to line measurements using a linear array camera as detection system. The performance of the LAC as detection system is characterized; potential issues are noted and possible solutions are offered. Initial demonstration of the approach has been shown in controlled conditions generated in a low-pressure (uniform properties) absorption cell, in a flat flame burner, and in the freestream of a supersonic wind tunnel. The initial low pressure measurements are shown to have good agreement with the traditional single line approach. The flat flame burner demonstrates the capability of the LAC to make profile measurements above the flame once the beam steering issue is resolved. Wind tunnel measurements are ongoing; a new setup is under design to reduce the room air contribution to the total measured signal that currently has limited a successful application of the method. A Monte Carlo analysis is used to explore the limits of validity of the planar measurements and data reduction method used in this work. This analysis can also be used to optimize absorption line selection for specific testing conditions, such as high temperature or low pressure applications.

## VII. Acknowledgements

This paper is based on work supported by the Air Force Office of Scientific Research under Grant No. FA9550-14-1-0396 with Dr. Chiping Li as Technical Monitor. The support of and discussion with Dr. Michael Brown at the Air Force Research Laboratory (AFRL) at Wright-Patterson Air Force Base is also acknowledged. JF acknowledges the support of the Department of Defense (DoD) through the National Defense Science and Engineering Graduate Fellowship (NDSEG) Program.

## References

- <sup>1</sup>Liu, X., Jeffries, J. B., and Hanson, R. K., "Measurement of Nonuniform Temperature Distributions Using Line-of-Sight Absorption Spectroscopy," *AIAA Journal*, Vol. 45, No. 2, 2007, pp. 411–419.
- <sup>2</sup>Chao, X., Jeffries, J. B., and Hanson, R. K., "Development of laser absorption techniques for real-time, in-situ dual-species monitoring (NO/NH<sub>3</sub>, CO/O<sub>2</sub>) in combustion exhaust," *Proceedings of the Combustion Institute*, Vol. 34, No. 2, 2013, pp. 3583–3592.
- <sup>3</sup>Schreier, F., "Optimized implementations of rational approximations for the Voigt and complex error function," *Journal of Quantitative Spectroscopy and Radiative Transfer*, Vol. 112, No. 6, 2011, pp. 1010–1025.
- <sup>4</sup>Rothman, L. S., Gordon, I. E., Babikov, Y., Barbe, A., Chris Benner, D., Bernath, P. F., Birk, M., Bizzocchi, L., Boudon, V., Brown, L. R., Campargue, A., Chance, K., Cohen, E. A., Coudert, L. H., Devi, V. M., Drouin, B. J., Fayt, A., Flaud, J. M., Gamache, R. R., Harrison, J. J., Hartmann, J. M., Hill, C., Hodges, J. T., Jacquemart, D., Jolly, A., Lamouroux, J., Le Roy, R. J., Li, G., Long, D. A., Lyulin, O. M., Mackie, C. J., Massie, S. T., Mikhailenko, S., Müller, H. S. P., Naumenko, O. V., Nikitin, A. V., Orphal, J., Perevalov, V., Perrin, A., Polovtseva, E. R., Richard, C., Smith, M. A. H., Starikova, E., Sung, K., Tashkun, S., Tennyson, J., Toon, G. C., Tyuterev, V. G., and Wagner, G., "The HITRAN2012 molecular spectroscopic database," *Journal of Quantitative Spectroscopy and Radiative Transfer*, Vol. 130, 2013, pp. 4–50.
- <sup>5</sup>Arroyo, M. P., Langlois, S., and Hanson, R. K., "Diode-laser absorption technique for simultaneous measurements of multiple gasdynamic parameters in high-speed flows containing water vapor." *Applied optics*, Vol. 33, No. 15, 1994, pp. 3296–307.
- <sup>6</sup>Arroyo, M. P. and Hanson, R. K., "Absorption measurements of water-vapor concentration, temperature, and line-shape parameters using a tunable InGaAsP diode laser." *Applied optics*, Vol. 32, No. 30, 1993, pp. 6104–6116.
- <sup>7</sup>Wheatley, B. J., McIntyre, T. J., and Buttsworth, D., "Tunable Diode Laser Absorption Spectroscopy of Hypersonic Flows," *19th Australasian Fluid Mechanics Conference*, 2014.
- <sup>8</sup>Lindstrom, C. D., Davis, D., Williams, S., and Tam, C.-J., "Shock-Train Structure Resolved with Absorption Spectroscopy Part II: Analysis and CFD Comparison," *AIAA Journal*, Vol. 47, No. 10, 2009, pp. 2379–2390.
- <sup>9</sup>Reid, J. and Labrie, D., "Second-harmonic detection with tunable diode lasers - Comparison of experiment and theory," *Applied Physics B*, Vol. 26, No. 3, 1981, pp. 203–210.
- <sup>10</sup>Goldenstein, C. S., Spearrin, R. M., Schultz, I. A., Jeffries, J. B., and Hanson, R. K., "Wavelength-modulation spectroscopy near 1.4  $\mu\text{m}$  for measurements of H<sub>2</sub>O and temperature in high-pressure and -temperature gases," *Measurement Science and Technology*, Vol. 25, No. 5, 2014, pp. 055101.
- <sup>11</sup>Fulge, H., Loehle, S., and Fasoulas, S., "Analysis of Wavelength Modulation Spectroscopy for Water Vapour Measurements in Supersonic Combustion," *11th AIAA/ASME Joint Thermophysics and Heat Transfer Conference*, , No. June, 2014, pp. 1–11.
- <sup>12</sup>Allen, M. G., "Diode laser absorption sensors for gas-dynamic and combustion flows." *Measurement science & technology*, Vol. 9, 1998, pp. 545–562.

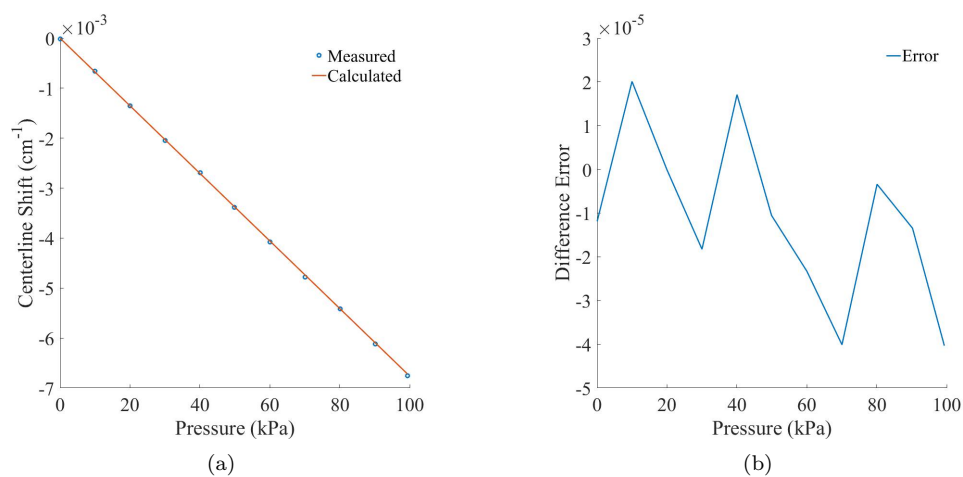


Figure 10. (a) Single line measured pressure shift superimposed on the calculated shift. (b) Difference error between the single line measured and calculated shifts.

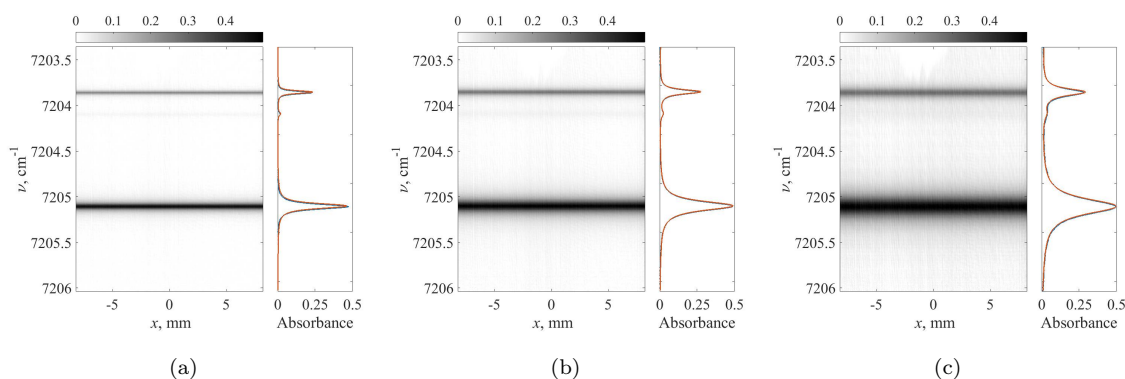


Figure 11. Spatial distribution of the spectral absorption across the measurement region (plane) taken through the low-pressure absorption cell at pressure of (a) 28.6 kPa, (b) 57.5 kPa, and (c) 98.3 kPa, with comparison of the line-averaged spectrum superimposed on the corresponding simulated spectrum (HITRAN).

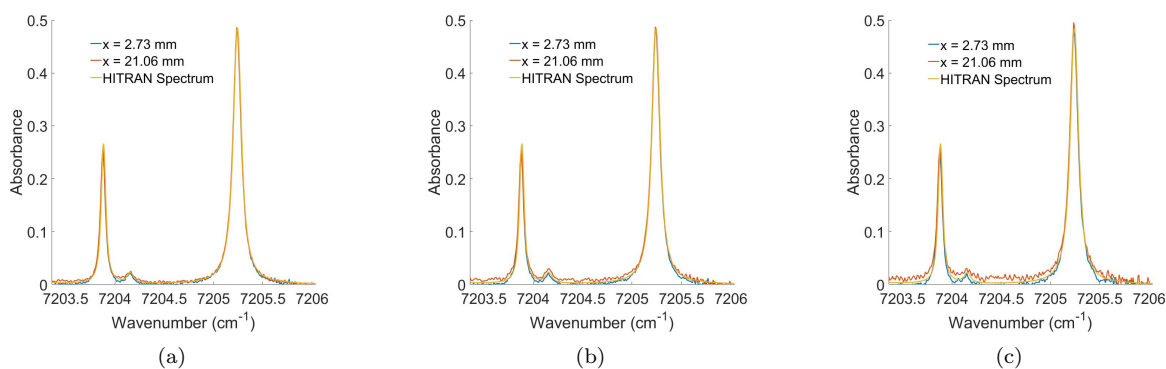


Figure 12. Spatially distinct, simultaneous spectra obtained from the linear array camera at two points on the plane ( $x = 2.73$  mm and  $x = 21.06$  mm) for (a) single pixels; (b) 5 pixel (0.124 mm) average; and (c) 10 pixel (0.248 mm) average.

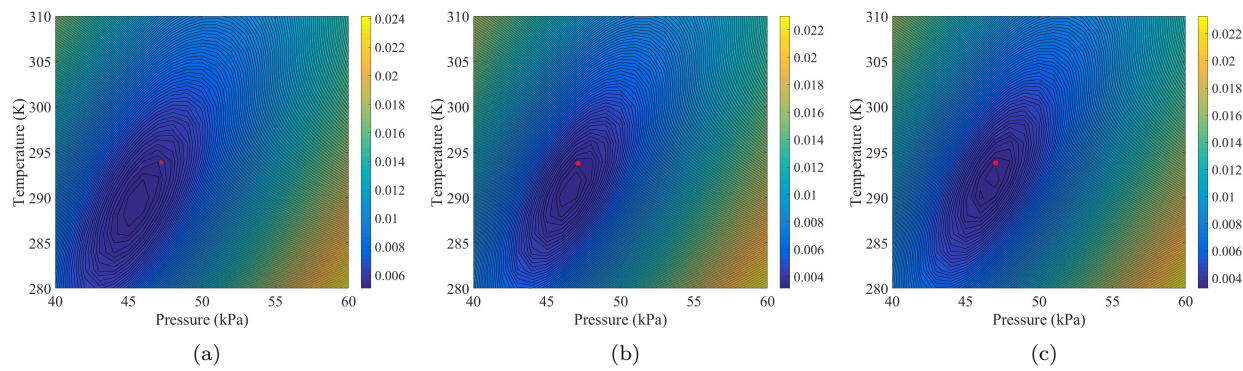


Figure 13. RMS error for the difference between the spectra measured by the LAC and the simulated HITRAN spectra with a  $\pm 5\%$  variation in fit temperature and a  $\pm 10\%$  variation in fit pressure for: (a) a single pixel, (b) a 5 pixel (0.124 mm) average, and (c) a 10 pixel (0.248 mm) average.

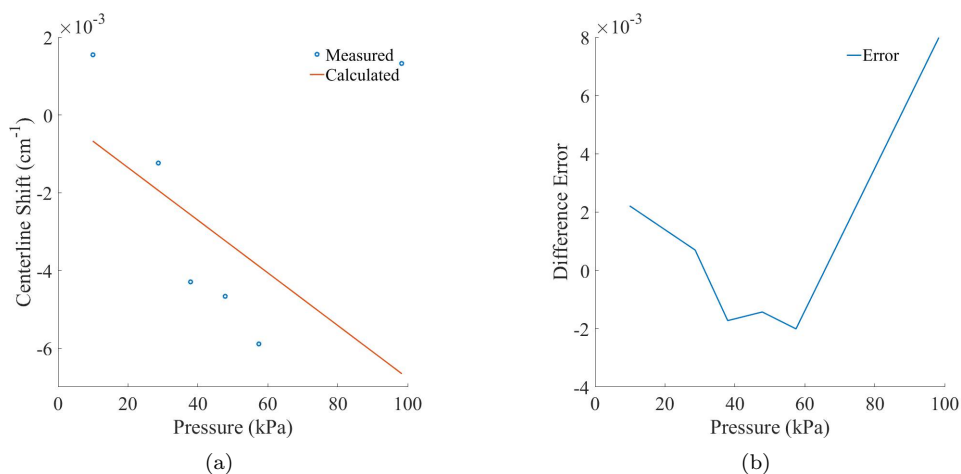


Figure 14. (a) LAC measured pressure shift superimposed on the calculated shift. (b) Difference error between the LAC measured and calculated shifts.

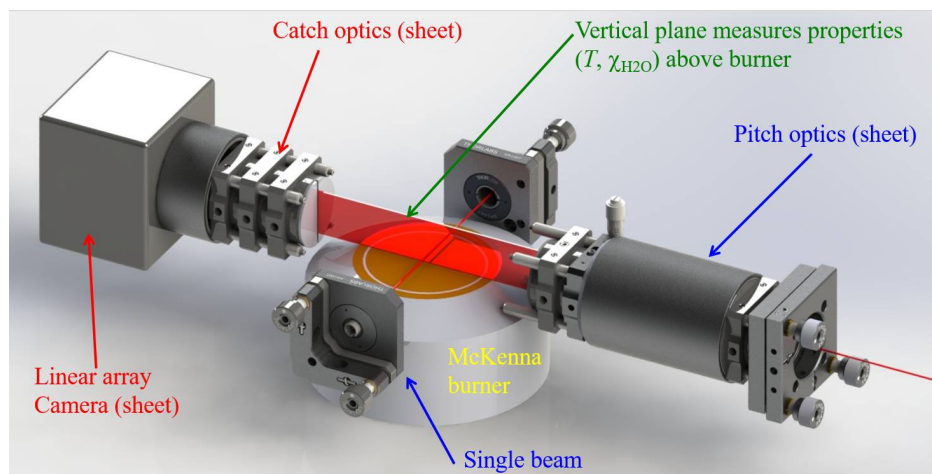


Figure 15. Schematic diagram of the flat flame McKenna burner experiment.

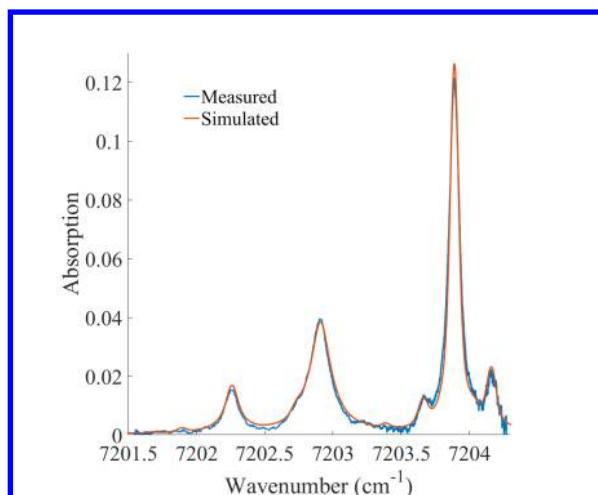


Figure 16. Spectral absorbance measured with the single line setup superimposed to a generated profile using both room and flame values to match the actual path measurement and a Voigt lineshape constructed with spectroscopic parameters from the HITRAN database.

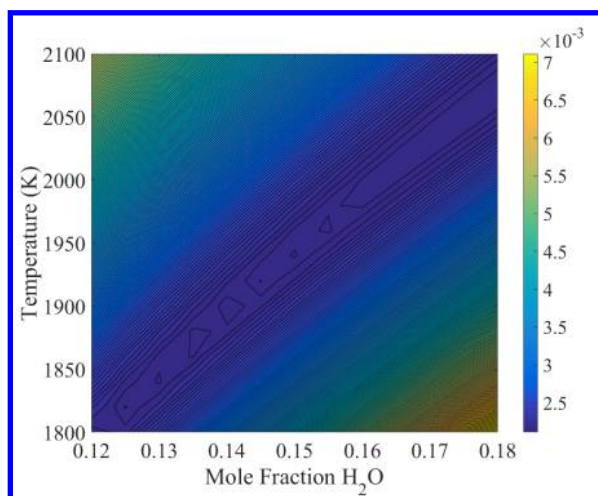


Figure 17. RMS error for the difference between the measured single line spectrum at 2.5 mm above the McKenna hydrogen/air flame and the HITRAN constructed spectrum for a range of temperatures and  $\text{H}_2\text{O}$  mole fraction.

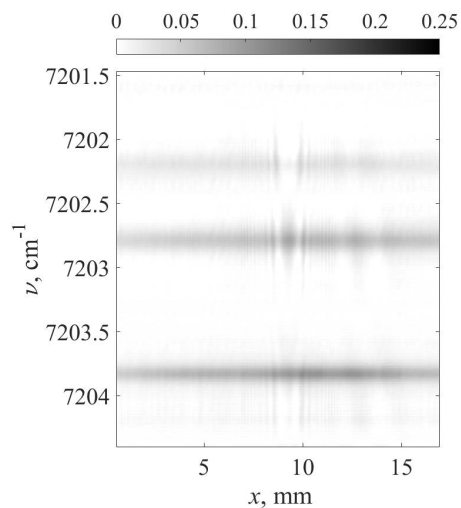


Figure 18. Spectral image taken above the burner surface with the plane oriented vertically. The spectrum on the right of the image is an average across the entire active area of the array.

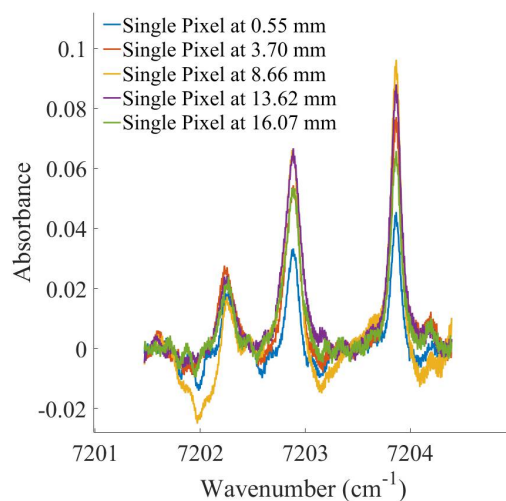


Figure 19. Single pixel spectra taken at different HAB locations. The variation in the spectra demonstrate the variation in temperature and species fraction above the burner.

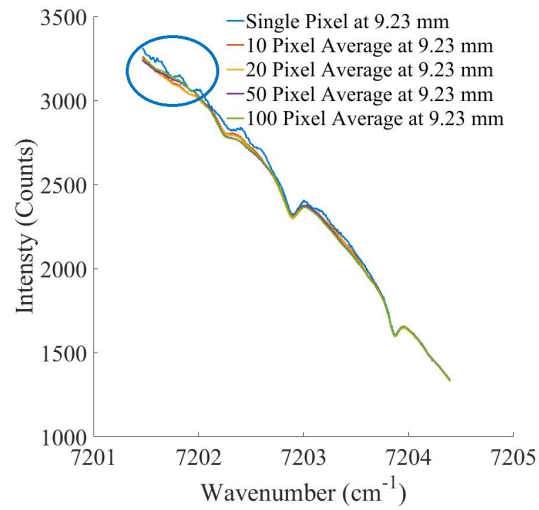


Figure 20. LAC camera traces for the single pixel, 10, 20, 50 and 100 pixel averages for the raw scan data centered at 9.23 mm above the burner.

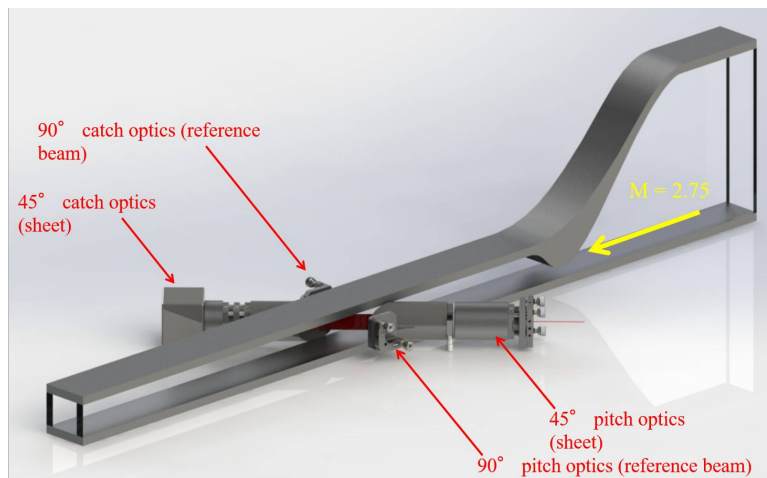


Figure 21. Schematic diagram of the Mach 2.75 wind tunnel experiment.

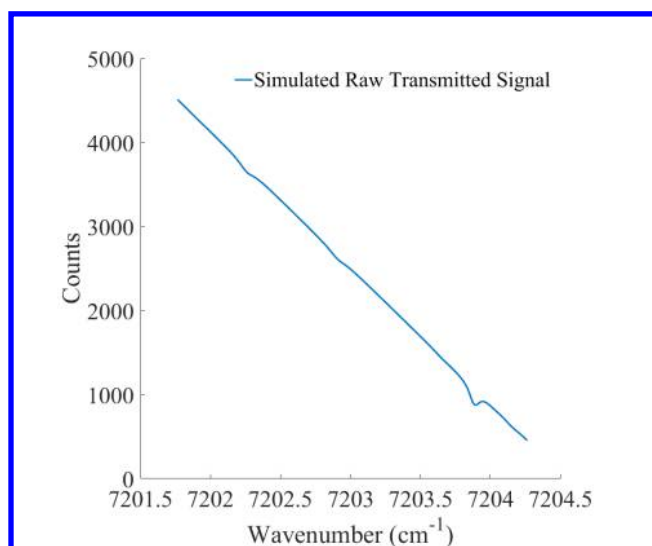


Figure 22. Simulated raw transmitted signal measured by the LAC.

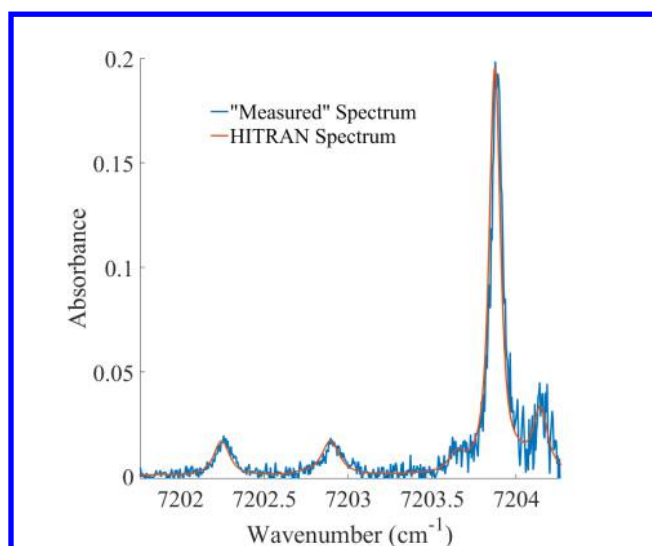


Figure 23. Synthetic “measured” spectrum superimposed on the HITRAN spectrum generated from the known values of pressure and temperature.

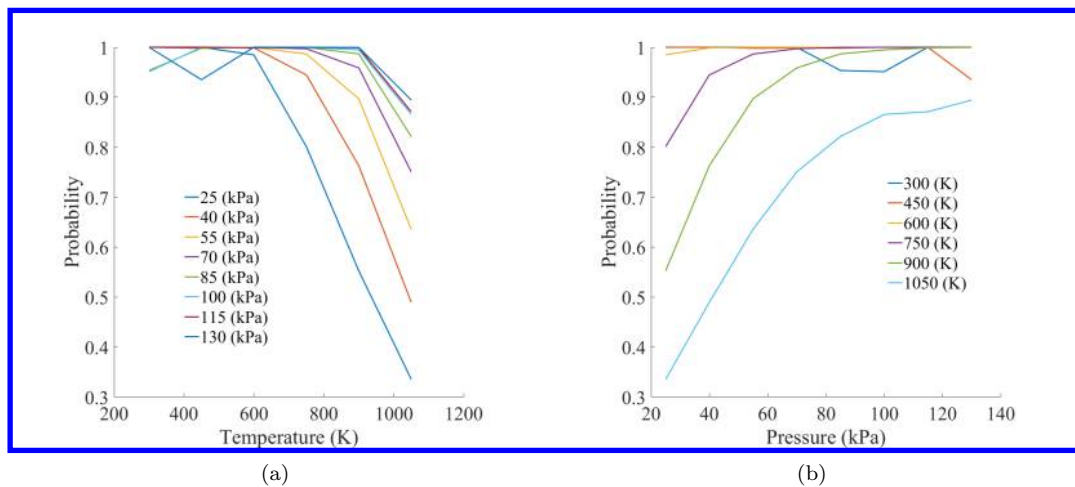


Figure 24. Probability that the reconstructed temperature error falls within 10% of the known value for cases (a) taken over a range of eight evenly spaced pressure values from 20 kPa to 130 kPa, binned by temperature; and (b) taken over a range of six evenly spaced temperature values from 300 K to 1050 K, binned by pressure.

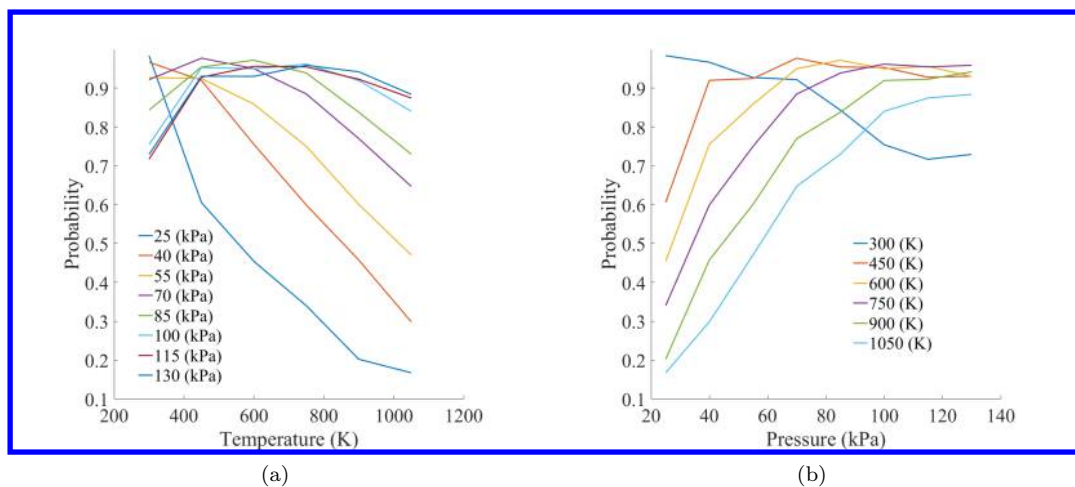


Figure 25. Probability that the reconstructed pressure error falls within 10% of the known value for cases (a) taken over a range of eight evenly spaced pressure values from 20 kPa to 130 kPa, binned by temperature; and (b) taken over a range of six evenly spaced temperature values from 300 K to 1050 K, binned by pressure.

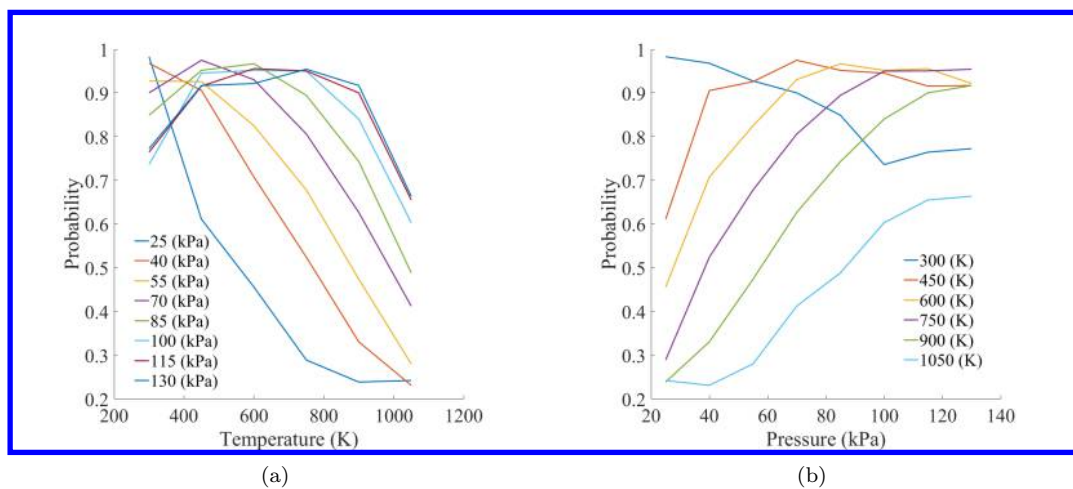


Figure 26. Probability that the reconstructed species mole fraction error falls within 10% of the known value for cases (a) taken over a range of eight evenly spaced pressure values from 20 kPa to 130 kPa, binned by temperature; and (b) taken over a range of six evenly spaced temperature values from 300 K to 1050 K, binned by pressure.

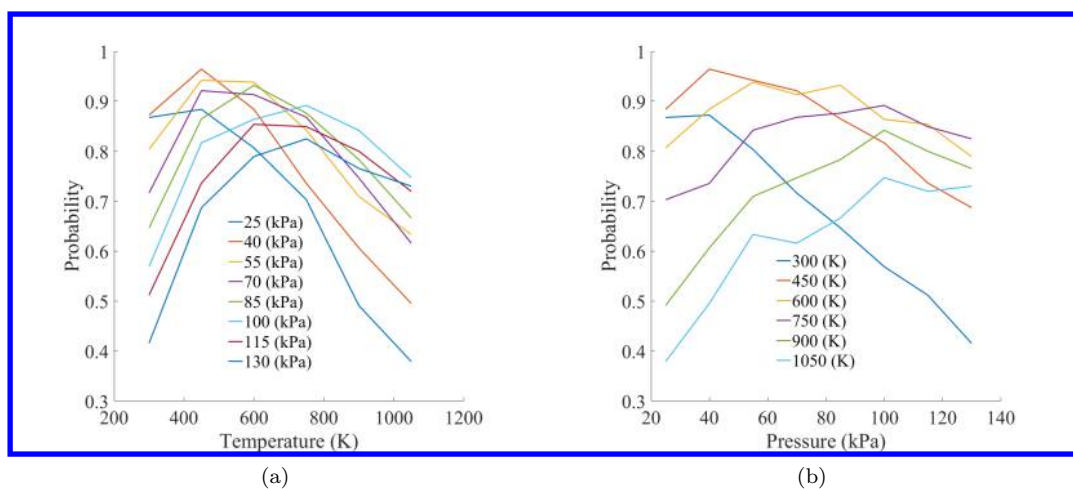


Figure 27. Probability that the reconstructed velocity error falls within 10% of the known value for cases (a) taken over a range of eight evenly spaced pressure values from 20 kPa to 130 kPa, binned by temperature; and (b) taken over a range of six evenly spaced temperature values from 300 K to 1050 K, binned by pressure.